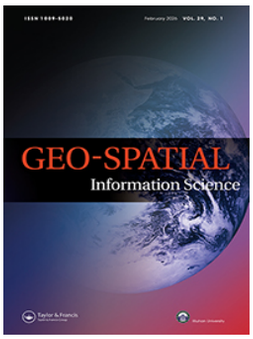

Geo-spatial Information Science

ISSN: 1009-5020 (Print) 1993-5153 (Online) Journal homepage: www.tandfonline.com/journals/tgsi20

Improving GNSS precise point positioning with tropospheric constraints from data-driven numerical weather prediction model

Yuanfan Deng, Wu Chen, Junsheng Ding, Ahmed El-Mowafy, Duojie Weng, Long Tang, Lei Bai & Xiaolong Mi

To cite this article: Yuanfan Deng, Wu Chen, Junsheng Ding, Ahmed El-Mowafy, Duojie Weng, Long Tang, Lei Bai & Xiaolong Mi (2026) Improving GNSS precise point positioning with tropospheric constraints from data-driven numerical weather prediction model, Geo-spatial Information Science, 29:1, 678-695, DOI: 10.1080/10095020.2025.2513650

To link to this article: https://doi.org/10.1080/10095020.2025.2513650

Published online: 12 Jun 2025.

GEO-SPATIAL INFORMATION SCIENCE
2026, VOL. 29, NO. 1, 678–695
https://doi.org/10.1080/10095020.2025.2513650

Taylor & Francis
Taylor & Francis Group

Improving GNSS precise point positioning with tropospheric constraints from data-driven numerical weather prediction model

Yuanfan Deng[a], Wu Chen[a], Junsheng Ding[a], Ahmed El-Mowafy[b], Duojie Weng[a], Long Tang[a,c], Lei Bai[d] and Xiaolong Mi[a]

[a]Department of Land Surveying and Geo-Informatics, The Hong Kong Polytechnic University, Hong Kong, China; [b]School of Earth and Planetary Sciences, Curtin University, Perth, Australia; [c]School of Civil and Transportation Engineering, Guangdong University of Technology, Guangzhou, China; [d]Shanghai Artificial Intelligence Laboratory, Shanghai, China

ABSTRACT

Accurate priori tropospheric knowledge is advantageous for Global Navigation Satellite System (GNSS) precise point positioning (PPP), which significantly influences both convergence time and the accuracy of tropospheric delay estimations. However, traditional numerical weather prediction (NWP) models, which are often used to provide this tropospheric information, rely heavily on parameterization. This reliance can introduce approximation errors and increase computational demands, limiting their effectiveness. In contrast, emerging data-driven NWP models offer enhanced forecasting capabilities with reduced computational requirements, presenting a promising alternative for improving PPP performance. This study proposes an innovative approach to improve PPP by leveraging data-driven NWP models. An evaluation involving nearly 20,000 stations reveals that these models outperform conventional NWP products, such as the Global Forecast System (GFS), achieving a 63% improvement in short-range zenith tropospheric delay (ZTD) forecast precision and a 55% enhancement in accuracy. For medium-range ZTD forecasts, data-driven NWP consistently surpasses GFS and even outperforms the empirical ZTD model GPT3 over a 15-day forecast period. Consequently, data-driven NWP facilitates a more rapid and accurate estimation of tropospheric random walk process noise (RWPN) compared to GFS. Moreover, validation with GPS kinematic positioning indicates that incorporating short-range ZTD forecasts as prior information reduces convergence time by an average of 400 s across 200 global stations, while medium-range forecasts also contribute positively when short-range data are unavailable. These findings demonstrate the potential of data-driven NWP models to improve tropospheric delay estimation and enhance PPP performance.

ARTICLE HISTORY
Received 12 January 2025
Accepted 27 May 2025

KEYWORDS
Global navigation satellite system (GNSS); zenith tropospheric delay; random walk processing noise; precise point positioning; numerical weather prediction

1. Introduction

The impact of tropospheric path delay caused by the neutral atmosphere on space geodetic applications, such as the Global Navigation Satellite System (GNSS), is significant, with errors reaching up to tens of meters at low elevation angles (Hackman et al. 2015; Hobiger et al. 2008). While tropospheric delay can be estimated accurately in precise point positioning (PPP) with random walk process constraints, PPP processing still requires tropospheric priori assumptions. Therefore, accurate priori tropospheric information is advantageous for PPP processing, as it directly affects positioning convergence time and tropospheric delay estimation accuracy as well as better height estimation (Huang et al. 2023; Li, Zhang, and Ge 2011; Wang and Liu 2019; Wilgan et al. 2017; Yao et al. 2017).

In current PPP applications, tropospheric delay – typically represented as the zenith total delay (ZTD), which is the sum of the zenith hydrostatic delay (ZHD) and the zenith wet delay (ZWD) – is handled primarily via empirical models and external corrections. Empirical models – such as the Hopfield (Hopfield 1969), Saastamoinen (Saastamoinen 1972), and Black (Black 1978) models – use standard meteorological parameters (e.g. from the Global Pressure and Temperature 3 (GPT3) model (Landskron and Böhm 2018)) to accurately model the ZHD; however, they struggle to capture the rapid temporal and spatial variations of the ZWD. To improve delay estimation, researchers have introduced external corrections from regional reference networks, which provide high accuracy and temporal resolution (Du et al. 2024; Xia et al. 2023; Zhang et al. 2022), and have employed GNSS tropospheric tomography to reconstruct 3D water vapor fields – thereby enhancing height accuracy and shortening PPP convergence time (Haji-Aghajany et al. 2021; Hurter and Maier 2013). In parallel,

CONTACT Xiaolong Mi xiaolong.mi@polyu.edu.hk

machine learning methods – such as long short-term memory (LSTM) networks (Haji-Aghajany et al. 2025) and back-propagation (BP) neural networks (Huang et al. 2024) – have been trained on historical GNSS-derived ZTD data for real-time tropospheric delay forecasting. For instance, Chen and Gao (2024) achieved ZTD predictions with an RMSE of around 2 cm – comparable to post-processed tropospheric estimates – while Zhang et al. (2022) obtained forecasts with 1 cm RMSE, shortening convergence time by up to 31% when used as a priori constraints in PPP. Despite these advances, these methods still exhibit limitations: empirical models and external corrections cannot fully capture rapid local variations, and techniques like tomography or LSTM-based predictions rely heavily on the availability of dense, local GNSS reference data, thereby restricting their applicability in regions with sparse instrumentation.

An alternative approach involves calculating tropospheric path delay directly using numerical weather prediction (NWP) models. By employing ray-tracing techniques through simulated atmospheric fields, NWP models offer extensive spatial coverage, continuity of service, and the potential for real-time application. Numerous studies have applied NWP models to generate prior tropospheric delay (Gao et al. 2024; Gong et al. 2024; Lu et al. 2017; Vaclavovic et al. 2017), and for offshore areas with sparse reference stations, Xu et al. (2025) proposed a regional augmented PPP algorithm that integrates NWP-derived delays with CORS network observations to significantly improve convergence and accuracy. Beyond delay estimation, accurately modeling tropospheric variation is critical. Typically, the tropospheric random walk process noise (RWPN) is assumed constant (ranging from 1 mm/$\sqrt{h}$ to 20 mm/$\sqrt{h}$, Zhang et al. 2023), yet its temporal and spatial variability indicates that such simplification is insufficient (Hadas et al. 2017). Although a global RWPN empirical model (GRM) has been proposed (Wu et al. 2023), directly estimating RWPN from NWP models remains more representative of the true atmospheric state. However, the need to numerically solve complex prognostic equations via spatial and temporal discretization imposes substantial computational costs (Bauer, Thorpe, and Brunet 2015; Ben Bouallègue et al. 2024) thereby limiting the practical use of traditional NWP approaches in real-time PPP.

In contrast, emerging data-driven NWP models offer enhanced forecasting capabilities with significantly reduced computational demands. Recent developments – such as Pangu-Weather, GraphCast, and FengWu, developed by Huawei, Google, and Shanghai Artificial Intelligence Laboratory, respectively (Bi et al. 2023; Chen et al. 2023; Lam et al. 2023) – demonstrate performance comparable to conventional NWP systems while enabling rapid processing. These models can generate accurate short-range and medium-range tropospheric delay forecasts and facilitate a more precise estimation of tropospheric RWPN, thereby capturing the dynamic water vapor variability with lower computational cost. This efficiency makes data-driven approaches highly promising for real-time PPP applications, especially in regions where dense reference networks are unavailable.

In this contribution, we propose to improve PPP performance by incorporating the tropospheric constraints derived from data-driven NWP model. We will evaluate the performance of data-driven NWP models when using short-range and medium-range tropospheric delay forecasting. The potential of determining tropospheric RWPN using data-driven NWP models will also be discussed. Through simulation experiments, we analyze what accuracy of tropospheric delay is required for improving PPP. Then, the derived tropospheric forecast products are applied in troposphere-weighted PPP approach. These results are next compared to the standard PPP method to validate the improvement of convergence time due to implementing augmented by data-driven NWP models.

2. Data-driven models and datasets

This section describes the selected NWP models and NWM data used in this study. While numerous global weather forecasting models exist, based on model availability and the variables used, we focus specifically on Pangu-weather, GraphCast and FengWu models.

2.1. Data-driven models

Pangu-Weather is a data-driven weather model which employs a specially designed three-dimensional Earth-specific transformer architecture (Bi et al. 2023). Integrating height information into a three-dimensional framework allows Pangu-weather to have higher accuracy gains in capturing the relationship between atmospheric states at different pressure levels. Pangu-Weather offers four distinct pre-trained models, each tailored to forecast time steps of 1, 3, 6, and 24 h. To generate forecasts for a given lead time, the predictions from the four different lead time models are combined autoregressively, utilizing the minimum number of steps necessary. This also implies that the model can offer a minimum temporal resolution of 1 h. However, Pangu-Weather has a limitation in that it only utilizes 13 pressure levels, which can potentially reduce the accuracy of integrating tropospheric delay.

On the other hand, GraphCast uses a graph neural network architecture with an encode-process-decode

configuration, taking as input the states of Earth's weather at time $t = 0$ and $t = 6$ h and predicts the state at t=6 h, which means the minimum temporal resolution is 6 h. As medium-range global weather models, both Pangu-weather and GraphCast can use their outputs as inputs autoregressively to predict for longer time periods. Table 1 shows the variables used in the Pangu-Weather and GraphCast models. As Table 1 shows, GraphCast incorporates a larger number of pressure levels than the Pangu-Weather model. This means GraphCast has a better advantage in terms of global tropospheric delay retrieval.

FengWu model, which is another vision transformer variant, applies a multi-modal and multi-task approach to solve the medium-range forecast problem. Similar to GraphCast, FengWu also utilizes two consecutive six-hour data frames as input. However, Chen et al. (2023) showed that, the FengWu model demonstrates higher forecast accuracy compared to the GraphCast model.

In summary, Pangu-Weather, GraphCast, and FengWu represent the current state of the art in AI-based global medium-range forecasting (0–10+ days). Table 2 summarizes these differences, highlighting each model's strengths and weaknesses (Haji-Aghajany et al. 2024). While all three use autoregressive deep-learning architectures trained on ERA5 reanalysis data, they differ in temporal resolution, vertical discretization, and uncertainty handling.

NWMs data

The fifth-generation European Centre for MediumRange Weather Forecasts (ECMWF) reanalysis (ERA5) dataset provides hourly data on the Earth's surface and upper-air parameters (Hersbach et al. 2020), covering the necessary variables required for the models from January 1940 to the present day (December 2024). In this research, the ERA5 dataset with 0.25°×0.25° (in latitude and longitude) spatial resolution is used as the initial condition of the data-driven NWP models, as well as the ground truth to evaluate the forecast precision. In addition, the operational National Centers for Environmental Prediction (NCEP) GFS forecast grids are analyzed, as a representative of the conventional NWP method, and compared to the data-driven NWP method (National Centers for Environmental Prediction et al. 2015). The GFS forecasts are on a global latitude-longitude grid with a 0.25° resolution, including forecast periods (time steps) at 3-h intervals up to 240 h, and 12-h intervals for the following prediction period from 240 to 384 h.

2.2. Empirical tropospheric delay and RWPN model

In the absence of external tropospheric corrections, the use of empirical models is the most common and convenient approach for mitigating the hydrostatic tropospheric delays in GNSS applications. In this research, we select the GPT3 model and the GRM model as the representative of empirical tropospheric delays and empirical tropospheric RWPN model, respectively, to analyze the advantages of data-driven NWP in comparison to widely used alternatives. The GPT3 model is an empirical tropospheric delay model that provides global-scale estimates of pressure, temperature, and ZHD based on spatiotemporal inputs (latitude, longitude, height, and time) (Landskron and Böhm 2018). The GRM model defines the optimal random walk process noise (RWPN) through a parametric equation combining temporal periodicity, height dependence, and spatial variation. Specifically, the RWPN at a reference height is modeled as:

Table 1. Weather variables and pressure levels modeled by Pangu-Weather, GraphCast and FengWu data-driven NWP models.

Surface variable	Atmospheric variables	Pressure levels (hPa)
2-m temperature	**Temperature**	1,2,3,5,7,10,20,30,**50**,70,**100**,12
10 m u wind component	**U component of wind**	5,**150**,175,**200**,225,**250**,**300**,35
10 m v wind component	**V component of wind**	0,**400**,450,**500**,550,**600**,650,**700**,
Mean sea-level pressure	**Geopotential**	750,775,800,825,850,875,900
Total precipitation	**Specific humidity**	,**925**,950,975,**1000**
	Relative humidity	
	Vertical wind speed	

Entries in bold correspond to Pangu-Weather, while entries with underlining correspond to FengWu.

Table 2. Comparison of key features of Pangu-Weather, GraphCast, and FengWu data-driven NWP models.

Model	Architecture	Temporal Resolution	Advantages	Disadvantages
PanguWeather	3D Vision Transformer	1 hour	Extremely fast inference; highest temporal granularity; lower compute cost	Coarse vertical resolution; no uncertainty output
GraphCast	Graph Neural Network (encode-process-decode)	6 hours	Rich vertical detail & variable coverage; captures large-scale patterns; ideal for delay modeling	Lower temporal resolution; deterministic only
FengWu	Multi-modal Vision Transformer	6 hours	Highest forecast accuracy; built-in uncertainty estimation; multimodal fusion	High computational cost; lower temporal resolution

$$\mathrm{RWPN}_0 = a_0 + a_1\cos\left(2\pi\frac{\mathrm{DoY}}{365.25}\right) + a_2\sin\left(2\pi\frac{\mathrm{DoY}}{365.25}\right) + a_3\cos\left(4\pi\frac{\mathrm{DoY}}{365.25}\right) + a_4\sin\left(4\pi\frac{\mathrm{DoY}}{365.25}\right) \quad (1)$$

where a_0 is the mean value, a_1 and a_2 represent annual amplitudes, and a_3 and a_4 denote semi-annual amplitudes. The station-specific RWPN is further adjusted for orthometric height (h) via an exponential function:

$$\mathrm{RWPN}_1 = \mathrm{RWPN}_0 \cdot e^{a_5 \Delta h} \quad (2)$$

where a_5 is a height coefficient and Δh is the elevation difference. Spherical harmonics (degree n=m = 12) are employed to globally represent the coefficients, enabling efficient interpolation without grid storage. This formulation captures spatiotemporal variations in water vapor, reducing ZTD estimation errors by >10% compared to fixed RWPN values (Wu et al. 2023).

2.3. GNSS ZTD products

The Nevada Geodetic Lab (NGL) has been providing GNSS tropospheric products for over 18,600 GNSS stations (Blewitt, Hammond, and Kreemer 2018). These products are provided on a daily basis, with a time interval of 5 min, and adhere to the International GNSS Service (IGS) SINEX_TRO standard. Each file includes various parameters such as total zenith delay, north gradient, east gradient, water vapor, and weighted mean temperature.

3. Method

This section begins with an overview of retrieving tropospheric delay from data-driven NWP. Then, the obtained priori tropospheric information is used to enhance PPP performance through the development of a troposphere-weighted approach and adaptive stochastic constraints. Figure 1 illustrates the overall methodological workflow: (1) generation of weather forecasts using data-driven NWP models, (2) retrieval of zenith tropospheric delay from NWP outputs, and (3) application of these delays as prior constraints in the troposphere-weighted PPP solution. All data-driven Numerical Weather Prediction (NWP) forecasts were generated on a central processing unit (CPU)-only high-performance computing (HPC) cluster, where each job could allocate up to 128 gigabytes (GB) of random-access memory (RAM) and individual compute nodes provided up to 36 CPU cores and 500 GB of RAM. Generating a ten-day forecast using CPU-only resources typically required several hours of computation.

3.1. Tropospheric delay retrieval from NWP

With a set of weather variables from ERA5 data at a specific time input as the initial condition, the NWP model can predict the input variables at a set time in the future. Once the predicted weather variables are obtained, by utilizing the meteorological parameters including the geopotential height, specific humidity and temperature of each pressure level, we can retrieve ZHD and ZWD by using the following integrations (Nilsson et al. 2013).

$$\begin{cases} ZHD_{\mathrm{nwp}} = \sum_{i=1}^{k-1}\left[\left(n_{h,i}^{z} - 1\right)\Delta h_i\right] \\ ZWD_{\mathrm{nwp}} = \sum_{i=1}^{k-1}\left[\left(n_{w,i}^{z} - 1\right)\Delta h_i\right] \end{cases} \quad (3)$$

where Δh_i is the height difference between each of two consecutive height levels of grid points. k is the

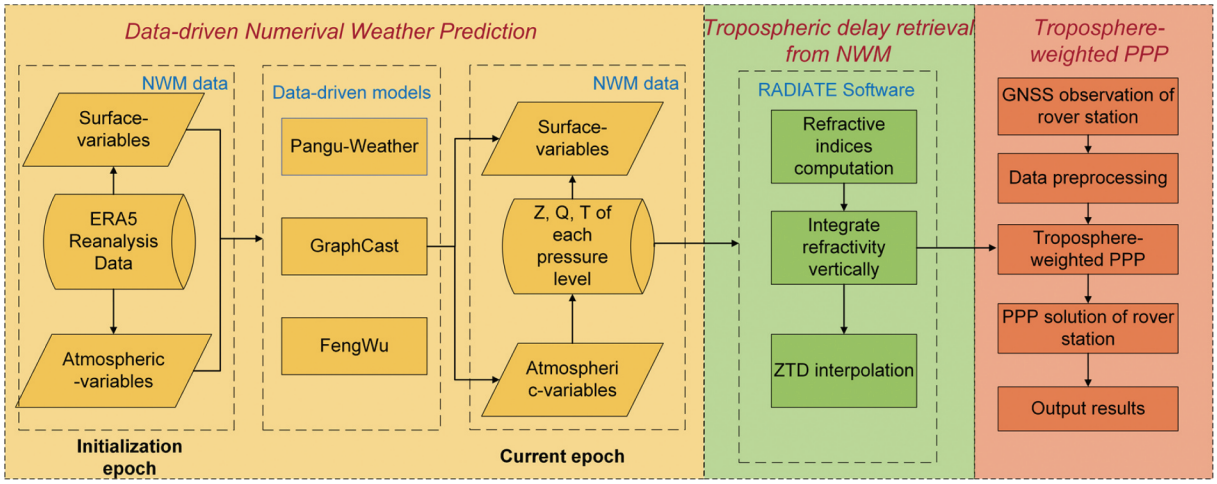

Figure 1. Overall processing workflow. The three colored blocks represent the data-driven NWP procedure (yellow), tropospheric delay retrieval from NWP (green), and troposphere-weighted PPP (red). Z, Q, and T denote geopotential height, specific humidity, and temperature, respectively.

number of heights, $n^z_{h,i}$ and $n^z_{w,i}$ are mean hydrostatic and wet refractive indices at the intermediate height between the two consecutive levels along the zenith direction. The refractive indices at exact horizontal points were bi-linearly interpolated using the refractive indices at grid points. The refractive indices at grid points were calculated as follows (Nilsson et al. 2013):

$$\begin{cases} n_h = 1 + k_1 \frac{p}{T} \times 10^{-6} \\ n_w = 1 + \left(k_2^{'} \frac{p_w}{T} + k_3 \frac{p_w}{T^2}\right) \times 10^{-6} \end{cases} \tag{4}$$

where T is the temperature in degrees K. $k_1, k_2^{'}$and k_3 are constants equal to 77.6890 K/hPa, 22.9742 K/hPa, and 375,463 K^2/hPa, respectively (Rüeger 2002). p denotes the total pressure, and water vapour pressure p_w can be converted from specific humidity q as follows (Nafisi et al. 2012):

$$p_w \approx \frac{qp}{0.622+0.378q} \tag{5}$$

In this research, the open-source ray-tracing software, RADIATE (Hofmeister 2016) is used to yield ZHD and ZWD, as it has been demonstrated to be computationally efficient given the complexity of the approach. We modify the original version to support flexible pressure levels configurations (according to Table 1 values, 13 levels for Pangu-Weather, 33 levels for GFS, and 37 levels for GraphCast and FengWu).

3.2. The standard PPP model

The standard undifferenced and uncombined PPP observation equations can be expressed as,

$$\begin{cases} P^s_{r,f} = \vec{e}^s_r \cdot \vec{x} + c(dt_r - dt^s) + T^s_r + \gamma_f I^s_{r,1} + c\left(d_{r,f} + d^s_f\right) + \varepsilon_{P,f} \\ L^s_{r,f} = \vec{e}^s_r \cdot \vec{x} + c(dt_r - dt^s) + T^s_r - \gamma_f I^s_{r,1} + \lambda_f N^s_{r,f} + c\left(b_{r,f} + b^s_f\right) + \varepsilon_{L,f} \end{cases} \tag{6}$$

where the indices s, r and f ($f = 1,2$) denote the satellite, receiver and frequency, respectively; $P^s_{r,f}$ and $L^s_{r,f}$ represent the raw code and phase observation; $\vec{e}^s_r$ is the unit vector from satellite to receiver; $\vec{x}$ is the receiver coordinates vector;c is the speed of light in vacuum; dt_r and dt^s are the receiver and satellite clock offsets, respectively; $I^s_{r,1}$is ionospheric delay along with the signal transmission path at the first frequency and $\gamma_f = f_1^2/f_f^2$ is the frequency-dependent multiplier factor; N_f is the phase ambiguity; $d_{r,f}$ and d^s_f are the frequency-related receiver and satellite code observation biases, and $b_{r,f}$ and b^s_f are the biases in phase observations; $\varepsilon_{P,f}$ and $\varepsilon_{L,f}$ are the sum of measurement noise and multipath error for code and phase, respectively. T^s_r denotes the slant tropospheric delay, which can be divided into hydrostatic and a wet component as follows

$$T^s_r = mf_h(e) \cdot ZHD_r + mf_w(e) \cdot ZWD_r \tag{7}$$

In which ZHD_r and ZWD_r denote the ZHD and ZWD of the receiver r, respectively, and $mf_h(e)$ and $mf_w(e)$ represent their corresponding mapping functions. e denotes the satellite elevation angle, from 0 degrees at the horizon to 90 degrees at zenith. Considering that ZHD normally can be accurately corrected by empirical equations, it is common only to estimate ZWD in the traditional PPP model. Therefore, the unknown parameter vector $\boldsymbol{X}$ to be estimated in the PPP model can be expressed as

$$\boldsymbol{X} = \left[\vec{x}, dt_r, ZWD_r, \bar{I}^s_{r,1}, \bar{N}^s_{r,f}\right]^T \tag{8}$$

where $\bar{I}^s_{r,1}$ and $\bar{N}^s_{r,f}$ represent reparametrized ionospheric delay and ambiguity, which are affected by $b_{r,f}$,b^s_f, $d_{r,f}$ and d^s_f.

3.3. The troposphere-weighted PPP model

Regardless of the specific model employed, the priori information on the troposphere delay can added as a virtual observation,

$$v_{zwd} = ZWD_r - ZWD_{model}, 0 \le \sigma_{model} \le \infty \tag{9}$$

where σ_{model}denotes the uncertainty of the used tropospheric model, which depends on model accuracy. when set $\sigma_{model} = 0$, it implies an assumption that the provided ZWD from the model is completely accurate, which is the case when uncertainty information is not provided by the model. This assumption leads to a distinction from the troposphere-weighted model to the troposphere-fixed model. Conversely, when $\sigma_{model} = \infty$, it indicates a lack of priori information about the troposphere. In this case, the model degrades to the troposphere-float model, where the estimation of tropospheric delay is not constrained by any specific prior knowledge.

3.4. Stochastic models for troposphere parameters

In GNSS data processing, it is normal to use random walk process to constrain ZWD estimation:

$$ZWD_r(t) = ZWD_r(t-1) + \omega_{zwd}, \omega_{zwd} \sim N\left(0, \varepsilon\sqrt{\Delta t}\right) \tag{10}$$

where t denotes the epoch number; ω_{zwd} is process noise; Δt d denotes time interval; ε represents the Random Walk Process Noise (RWPN) of ZWD parameter, which can be estimated using the theory of Markov processes (Hadas et al. 2017):

$$E(\varepsilon) = \frac{\left|ZWD^t - ZWD^{t+\Delta t}\right|}{\sqrt{\Delta t}} \tag{11}$$

RWPN is normally set as a constant value, but deriving it from NWM data using Equation (11) can significantly enhance the convergence and accuracy of ZWD results. According to (Z. Zhang et al. 2023), the dynamic model achieves an inner accuracy of 4 mm, showing an improvement of at least 55.5% over the fixed RWPN model.

4. Accuracy evaluation of the models

In this section, the accuracy and precision of ZTD obtained from data-driven NWP are assessed through by comparing them with GNSS-ZTD and ERA5-ZTD, respectively. In addition, the RWPN values derived from NWP are also evaluated. To ensure a comprehensive analysis, we collect tropospheric product data from nearly 20,000 global GNSS stations available on the NGL sites, resulting in a large sample size for evaluation. Comparisons are conducted at common epochs and avoid interpolation effects due to the different sampling intervals of the data sources.

4.1. Short-range ZTD forecast

We initially investigate the performance of data-driven NWP for short-range ZTD forecasts with a 6-h time step. The accuracy of GFS, Pangu-Weather, GraphCast, and FengWu forecasts is assessed by comparing them with ERA5-ZTD and GNSS-ZTD. Table 3 presents the evaluation metrics of each model, including mean Root Mean Square Error (RMSE), Mean Absolute Error (MAE), and Bias relative to ERA5-ZTD, and GNSS-ZTD, respectively. Our analysis reveals that FengWu and GraphCast exhibit significant improvements compared to GFS, with a reduction in RMSE from 9.8 mm to 4.13 mm and 3.59 mm, respectively. GraphCast shows slightly better performance than FengWu, which may be attributed to GraphCast, incorporating total precipitation as an additional variable during model training. Pangu-Weather, however, underperforms with ERA5-ZTD RMSE of 13.02 mm and a large negative Bias (−8.36 mm), likely due to its coarse pressure levels. In terms of forecast accuracy, considering a difference of 10.1 mm between GNSS-ZTD and ERA5-ZTD (Zhou et al. 2020), the data-driven NWP models demonstrate a significant improvement of approximately 55% in forecast accuracy compared to GFS. As indicated by (Elsobeiey 2020; H. Li et al. 2023), there is potential to further reduce this difference through better modeling approaches.

Furthermore, Figure 2 presents the statistics and distribution of ZTD forecast residuals for each model on distinct dates, i.e. the first of the month for 1 year. The results of FengWu and GraphCast models demonstrate comparable performance, with ZTD residuals exhibiting an interquartile range (IQR) of less than 10 mm and a nearly zero-mean normal distribution, indicating unbiased forecast ZTDs. GFS also exhibits a zero-mean normal distribution but with a larger spread or variability in the ZTD residuals compared to FengWu and GraphCast. Pangu-Weather's error distribution shows a noticeable bias, particularly during the period from June to November, which can be attributed to the employed coarse pressure levels.

To further analyze the temporal and spatial characteristics of short-range forecast errors, we define a forecast error greater than 2 cm as an abnormal value, based on monitoring empirical data, and then count the number of stations with a large error at different dates and latitude ranges. As shown in Figure 2, it is evident that both in the southern hemisphere and the northern hemisphere, the number of abnormal stations is considerably higher in summer compared to winter. This can be attributed to higher temperatures during summer leading to increased surface evaporation and significant variations in water vapor, making it more challenging to accurately predict weather variables. Figure 3 illustrates that the polar region exhibits the lowest ratio of large errors to the total number of errors, followed by the tropics, while the mid-latitude region shows the highest ratio. This can be attributed to the low average temperatures in the polar region, leading to minimal water vapor content and making predictions comparatively easier. Although the tropical region experiences higher temperatures, resulting in a higher water vapor capacity in

Table 3. Evaluation metrics of ZTD 6-h forecast for using GFS, Pangu-Weather, FengWu, and GraphCast models, referenced to ERA5-ZTD, and GNSS-ZTD, respectively (in mm).

Model		ERA5		GNSS		
Metric	RMSE	MAE	Bias	RMSE	MAE	Bias
Pangu-Weather	13.02	7.26	−8.36	17.27	13.78	−10.14
GFS	9.80	7.26	0.30	11.03	8.51	−2.03
FengWu	4.13	3.07	−0.05	10.50	8.08	−1.95
GraphCast	3.59	2.69	−0.06	10.50	8.05	−1.96
ERA5	–	–	–	10.10	7.95	−1.88

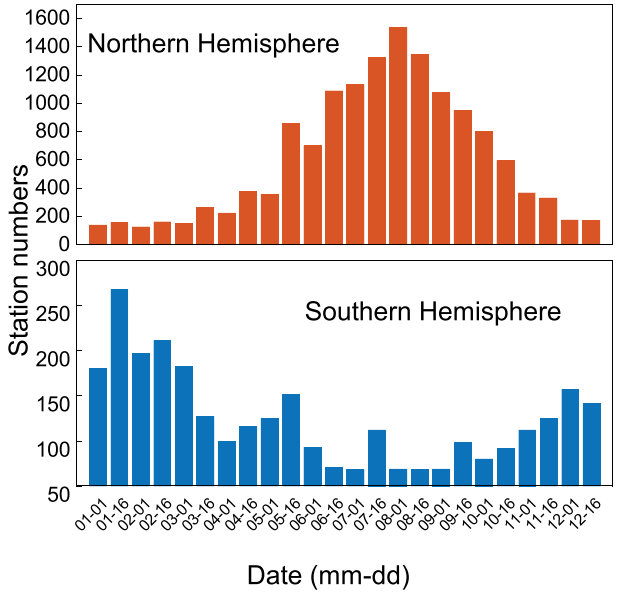

Figure 2. Numbers of stations with large error of short-range forecast ZTD (exceeding 2 cm) at different dates in 2022.

the atmosphere, the consistent and stable nature of its temperature, makes the water vapor levels steady and easier to predict (Hartmann and Michelsen 1993). In contrast, mid-latitude region undergoes seasonal temperature changes, which makes it challenging to predict the water vapor level in the atmosphere (Wu et al. 2023).

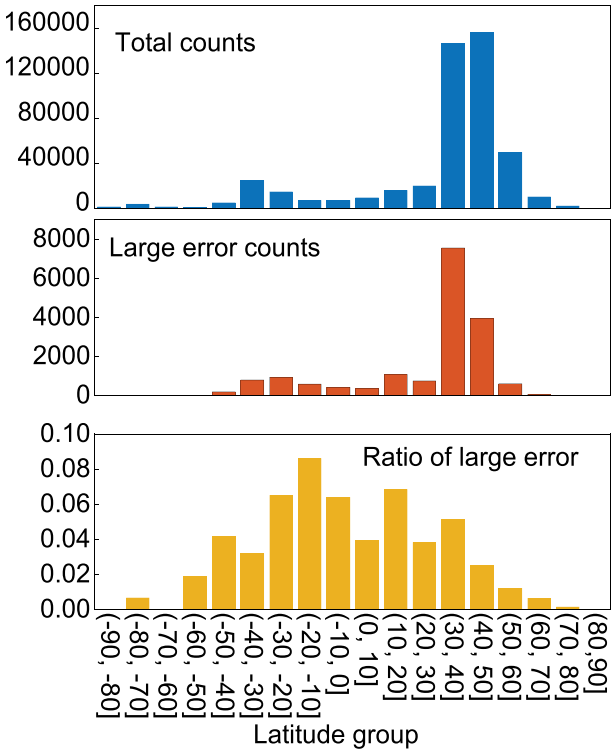

Figure 3. Total counts, large error (exceeding 2 cm) counts, and ratio of large error of short-range forecast ZTD in 24 datetimes for different latitude range.

The above analysis shows that the initial weather conditions correlate with tropospheric delay forecasting. Therefore, we further analyzed the relationship between ZWD forecast residuals and local weather variables to better understand their relationship. We focus on ZWD rather than ZTD, because the hydrostatic portion of ZTD is largely constant and would dilute the correlations with changing weather parameters. Considering the fact that atmospheric surface layer plays the main role in the formation of the tropospheric delay fluctuations (Khutorov et al. 2016), here we choose surface weather parameters sourced from the ERA5 dataset for analysis, including near-surface air temperature (2 m temperature), evaporation, total column water vapor (TCWV), and total column water vapor rate. It should be noted that, in the ECMWF Integrated Forecasting System (IFS), the convention is that downward fluxes are represented by positive values. Therefore, negative evaporation values indicate evaporation, whereas positive values indicate condensation. Taking GraphCast results shown in Figure 4 as an example, according to the residual range, the global ZWD forecast residuals were divided into 6 groups ranging from 0 to 10 mm in 2 mm range of each group, with the sixth group being 10 mm and above. Figure 5 presents the mean values of weather variables for each ZWD forecast residual group, showing that initial temperature, evaporation, TCWV, and TCWV rate increase with higher residual groups. The *X*-axis represents ZWD residual groups (grouped by magnitude in mm), while the *Y*-axis values correspond to different meteorological variables, as indicated in the legend with their respective units. These results can be explained by the fact that the forecast residuals are highly related to the convection development. Convective cells develop more readily with increasing surface temperature, transporting water vapor away from the Earth's surface (Khutorov et al. 2016). This corresponds to increased fluctuations in the phase of GNSS signals, i.e. the GNSS observations, making the delays harder to predict accurately.

4.2. Medium-range ZTD forecast

To analyze the performance of data-driven NWP in medium-range ZTD forecasts, we assess Pangu-Weather, GFS, GraphCast and FengWu forecast accuracy with 15 days forecast period, whose inference starts on 1st and 16th of each month in 2022. We calculate ZTD mean RMSE with an interval of 6 h and show it in Figure 6. The ZTD derived from GFS model, empirical model GPT3 and ERA5 are also compared at the same stations as in the previous section.

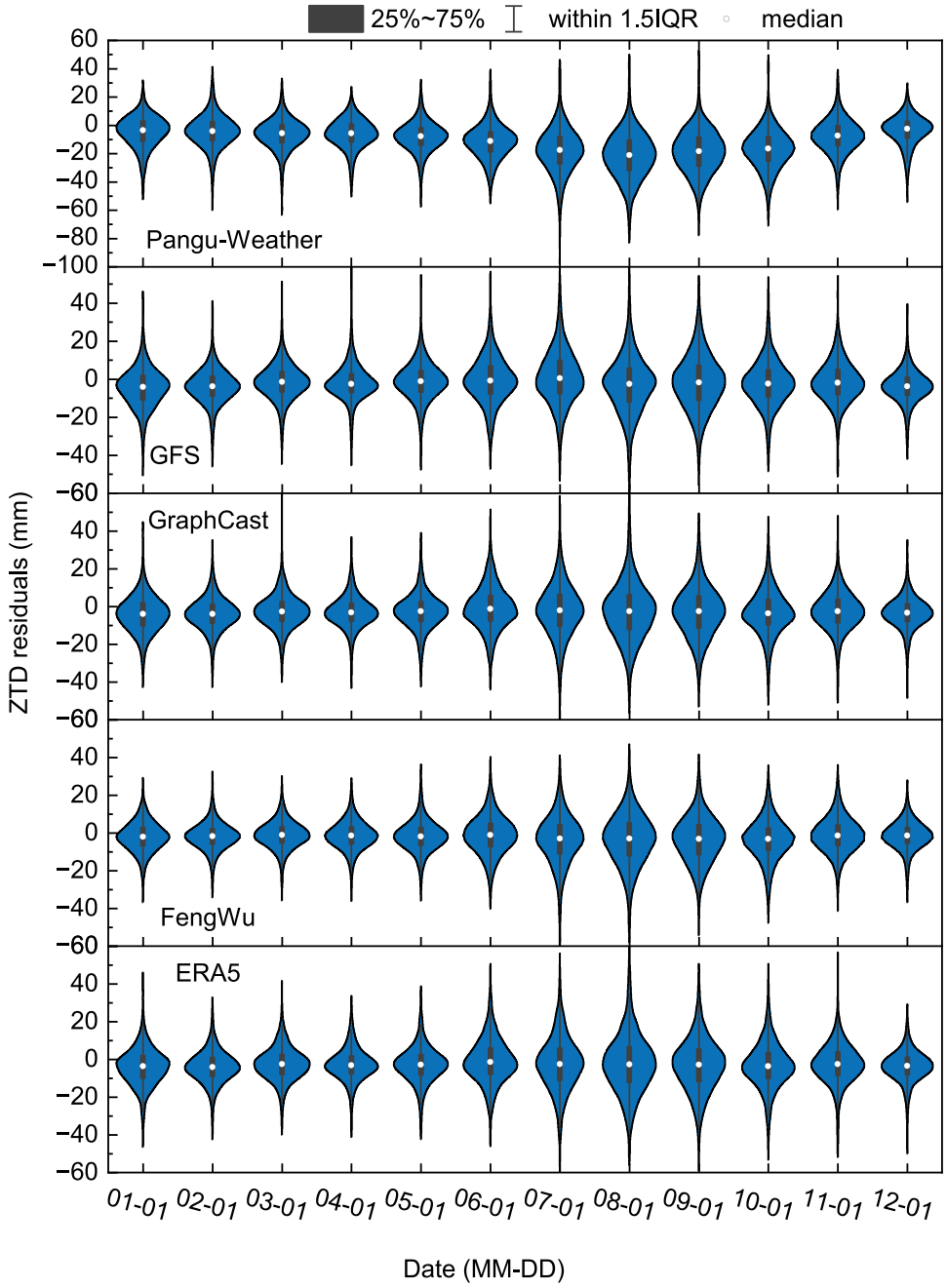

Figure 4. Violin plot of the short-range forecast ZTD residuals based on GNSS-ZTD for Pangu-Weather, GFS, FengWu, and GraphCast models on different dates in 2022. ERA5-ZTD residuals are also plotted for comparison. It shows the median values within 1.5 IQR, and the 25%-75% percentiles.

As shown in Figure 6, the mean RMSE of ZTD_{ERA5} is approximately 10 mm, which aligns with findings from previous studies evaluating ZTD_{ERA5} using ZTD_{GNSS} (e.g. Zhou et al. 2020). The RMSE of ZTD_{ERA5} at 00z (where 00z denotes 00:00 UTC in Zulu convention) may be slightly higher, which could be attributed to the processing strategy of ZTD_{GNSS} products (e.g. restarting at the beginning of each day and requiring PPP convergence time). Limited by the coarse pressure levels. The accuracy of $ZTD_{Pangu\text{-}Weather}$ is worse than that of $ZTD_{GraphCast}$ and ZTD_{FengWu} by 5 ~ 10 mm. FengWu and GraphCast exhibit higher forecast performance compared to GFS, and this improvement becomes more pronounced as the forecast period increases. The accuracy of $ZTD_{Pangu\text{-}Weather}$, ZTD_{GFS} degrades to a level comparable to that of ZTD_{GPT3} on the 9th day, while $ZTD_{GraphCast}$ reaches this level on the 13th day. In contrast, ZTD_{FengWu} is always better than GPT3 even after 15 days long forecast period. The forecast accuracy of $ZTD_{GraphCast}$ and ZTD_{FengWu} remains within the threshold of 20 mm for up to 4 days, whereas ZTD_{GFS} maintains accuracy for 3 days. GraphCast and FengWu shows similar forecast performance with an accuracy of 12 mm within 24 h. However, as the forecast time increases, FengWu outperforms GraphCast indicating that FengWu has a better medium-range forecast capabilities.

4.3. RWPN estimation

According to Equation (11), NWP models can derive relatively accurate dynamical RWPN values. In this section, we compare the RWPN determination performance between different RWPN setting strategies, including data-driven NWP models. The fixed RWPN values range from 1 to 10 mm/$\sqrt{h}$ (in intervals of 1 mm/$\sqrt{h}$) and the RWPN values calculated using GRM, taking RWPN derived from GNSS ZTD products as a reference. Figure 7 shows a 4 mm/$\sqrt{h}$ RWPN estimation error between the NWMs model results and GNSS ZTD products. The RWPN estimation accuracy of data-driven NWP models degrades to that of GRM empirical model at the fourth day, indicating that only short-range forecast can describe water vapour variation accurately. The best fixed RWPN value is 5 mm/$\sqrt{h}$, which is in agreement with the empirical value used in the previous research (Kouba and Héroux 2001; Wu et al. 2023). The GRM outperforms the best fixed RWPN value, but the improvement is limited, at only 0.17 mm/$\sqrt{h}$. In contrast, short-range data-driven NWP has demonstrated accuracy improvements approaching 2 mm/$\sqrt{h}$. The GRM was proposed with the aim of reducing computation load, while the transition from conventional NWP models to data-driven NWP models has already resulted in significant reductions in the computational needs. Therefore, it is recommended to incorporate the RWPN estimation process into the data-driven NWP framework.

5. Accuracy required for improving PPP in simulation

The use of precise external tropospheric constraints can improve PPP convergence; therefore, it is crucial to explore the impact of their accuracy on PPP. The constraint is treated as a virtual observation where its σ_{model} value is contingent on its precision, making it possible to analyze the precision by examining σ_{model}. To determine the impact of σ_{model} on PPP parameter estimation, we simulate the ground truth of troposphere delay and adjust its σ_{model} to analyze the resulting parameter estimation performance.

The details of this experiment are summarized in Table 4, where one-day of observation data from multi-GNSS capable stations were used with consistent satellite geometry. To obtain the ground truth, the tropospheric delay was estimated in the PPP coordinate-fixed mode, with the first 2 h of results removed to allow for PPP convergence. The PPP coordinate-kinematic mode constrained with the simulated tropospheric ground truth was then restarted every 2 h to calculate performance indicators, which include the mean convergence time, the ZWD post-convergence standard deviation (STD), the post-convergence STD of coordinates in east (E), north (N) and up (U) direction, where the mean value is taken after convergence. Here, we define "convergence" as achieving a 3D positioning error of less than 10 cm at the current epoch and the subsequent 10 min.

With σ_{model} set as the independent variable, using a log10 scale ranging from 1 mm to 10 m, the variation of different performance indicators of troposphere-weighted PPP is shown in Figure 8. In addition, the performance indicators of troposphere-float PPP are plotted in dash line for the sake of comparison. We can see that the impact of increasing tropospheric constraint accuracy leads to a clear deterioration effect. The post-convergence STD of ZWD, up-component coordinates shows to be a monotonically increasing function of σ_{model}, while that of east, north component little has changed, indicating that tropospheric constraints contribute mainly to vertical direction as expected. This can be attributed to the strong correlation between the height parameter and ZTD (Dodson et al. 1996). Nevertheless, the improvements in post-convergence STD remained limited to only a few millimeters, suggesting that the effects of tropospheric constraints after convergence are relatively minor. The convergence time also exhibits a monotonous increase as σ_{model} increases, with some observed variations. When σ_{model}reach a threshold of 10 cm, the convergence time and post-convergence STD of ZWD and U direction remain close to the level of the output of troposphere-float model, indicating that constraints imposed by the virtual observation become meaningless when the accuracy of tropospheric products is worse than 10 cm. Therefore, external tropospheric data is most useful to kinematic PPP users when accuracies are provided and are at least below 10 cm. Conversely, when σ_{model} is smaller than a few millimeters, the two dependent variables closely resemble the troposphere-fixed model. In this scenario, the improvement in convergence time can range from 20% to 30%, around 640 s on average, reflecting the maximum impact of the troposphere on PPP parameter estimation. Additionally, results showed that when σ_{model} was set to 2 cm, the mean reduction in convergence time was approximately 490 s.

6. Positioning verification

In this section, we will compare the performance of troposphere-weighted PPP with traditional PPP. Since PPP performance is not sensitive to tropospheric constraint improvements of just a few millimeters, as shown in the previous simulation experiment, we apply the data-driven predicted tropospheric delay only to the troposphere-weighted PPP. The positioning process strategy is the same as in Table 4, except that the satellite system used is GPS-only and the priori ZHD and ZWD derived from NWP. GraphCast was selected from the NWP model due to its best short-range forecast accuracy and accessibility of source code.

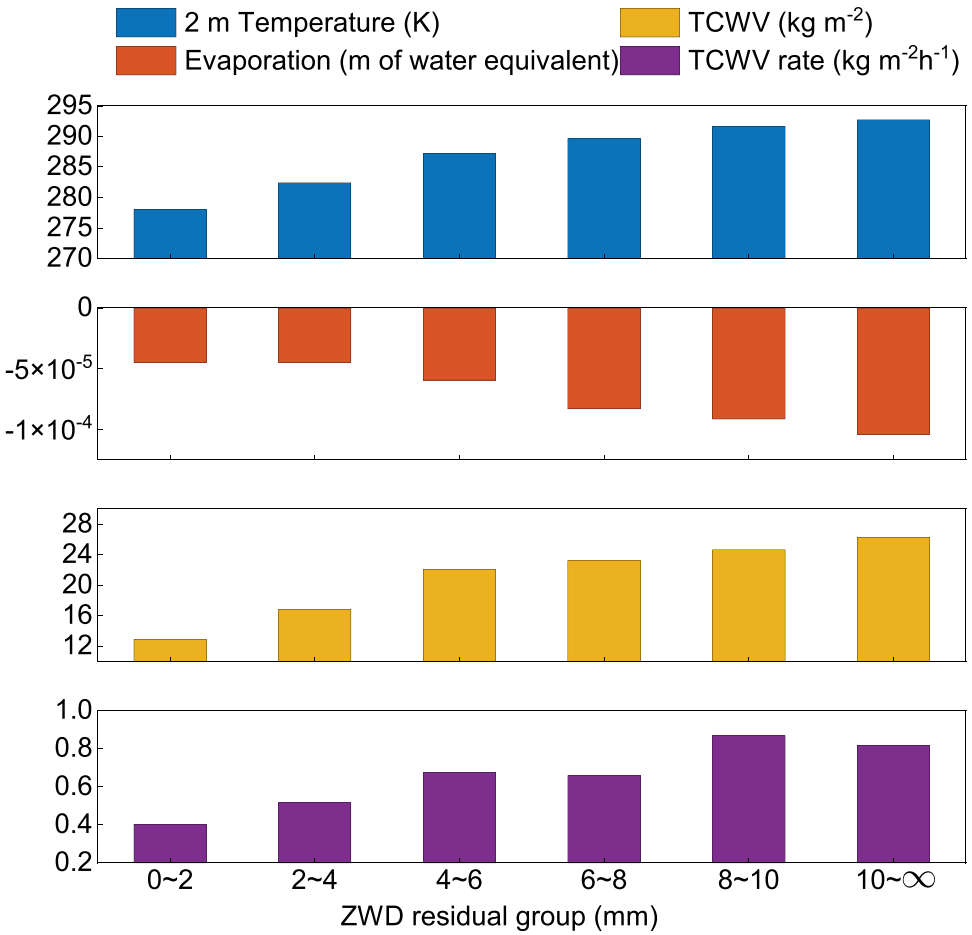

Figure 5. Relationship between ZWD forecast residual and local weather variables, with panels from top to bottom representing 2m temperature (K), evaporation (meters of water equivalent), total column water vapour (kg/m^2), and total column water vapour rate (kg/m^2/h) at the time of inference.

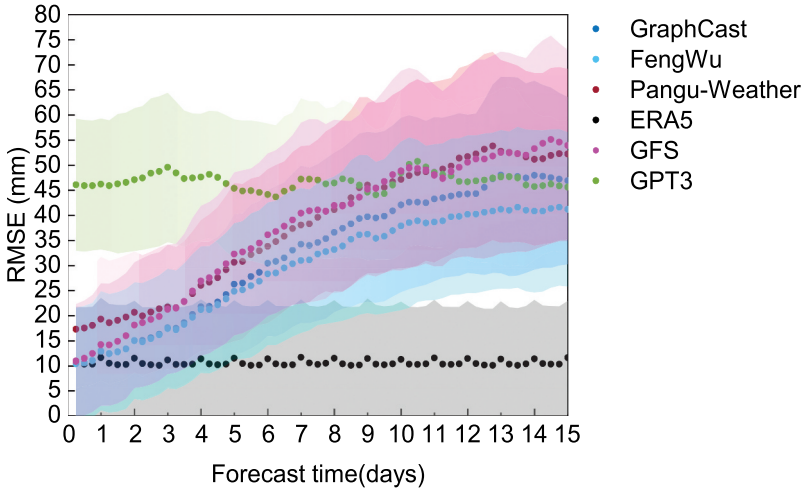

Figure 6. Mean RMSE of all stations referenced to GNSS ZTD products with a forecast over 15 days, with 6-hour intervals, for Pangu-Weather, FengWu and GraphCast 6-hour model. The shadowing area represents the variability (standard deviation) of the RMSE across all stations, highlighting the consistency of errors among different locations. GFS, ERA5 and GPT3 empirical models are plotted as a comparison.

6.1. PPP augmented by short-range forecast

In general, short-range NWP can provide accurate troposphere prior information. Therefore, we first make use of 6 h and 12-h forecast intervals starting at 00z to examine the performance of troposphere-weighted PPP. Due to the 6-h temporal resolution of GraphCast, additional linear interpolation was

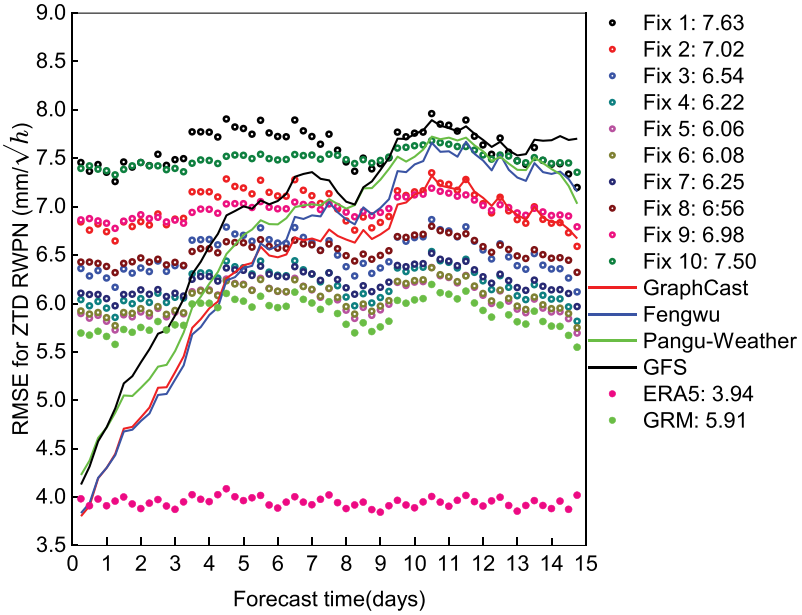

Figure 7. Mean RMSE for ZTD RWPN derived from the GFS, Pangu-Weather, FengWu, GraphCast and GRM models for 15 days forecast (60 intervals, with processing times in each day at 00z, 06z, 12z and 18z), with GNSS ZTD RWPN as the reference. The mean RMSE for each processing strategy are shown in the legend.

Table 4. PPP strategy when experimenting changing the σ_{model}value.

Item	ZTD estimation	PPP
Mode	PPP fixed	PPP kinematic
Signals	GPS L1/L2, Galileo E1/E5a, BDS-2 and BDS-3 B1I/B3I	
Sampling rate	30 seconds	
A priori noise	code: 0.3 m, phase: 0.003 m	
Elevation cut-off angle	10°	
Weighting	A function of the satellite elevation angle	
Satellite orbits and clocks	Rapid products provided by Wuhan University (WUM)	
Tropospheric mapping functions	Global mapping functions	
Ionospheric delay	Estimated with a random walk noise model ($0.04\ m/\sqrt{s}$)	
Tropospheric delay	ZHD: corrected (Saastamoinen) ZWD: estimated with a random walk noise model ($10^{-4}\ m/\sqrt{s}$)	ZHD: corrected (Saastamoinen) ZWD: estimated with a random walk noise model ($10^{-4}\ m/\sqrt{s}$) and constrained by a prior ZWD
Receiver coordinates	Fixed as PPP static solution	Estimated as white noise without any time correlations considered

performed between the 6-h batches to provide continuous tropospheric delay constraints. Based on the evaluation in previous sections, we set σ_{model} of short-range forecast as 2σ (set as 2 cm). However, some outliers may exist within the forecasted tropospheric delays, which may not improve positioning performance and could even lead to its degradation.

Taking the stations KERG and KOKB as representative examples, one constrained with good accuracy of tropospheric delay and the other with poor accuracy, their time series of positioning errors are depicted in Figure 9. As shown in the bottom panel of Figure 9 and taking ZWD series from GNSS products as a reference, the RMSE of ZWD from GraphCast interpolation at station KERG is 9.6 mm, while that at station KOKB is 39.4 mm. Accordingly, the improved effect of troposphere-weighted PPP compared to standard PPP is quite different. For KERG, significant reductions in the convergence time can be observed in the east, north and up directions when using troposphere-weighted PPP compared to the standard PPP. Troposphere-weighted PPP takes approximately 45 min to converge, whereas the standard PPP takes about 1.75 h, showing an improvement of 1 h. After convergence, the positioning accuracy of two schemes are comparable, and there is no evident improvement for troposphere-weighted PPP compared to standard PPP. That is reasonable if we acknowledge that the accuracy of ZTD estimation can reach up to mm level after PPP convergence, while the added tropospheric constraints are set at 2 cm. As for station KOKB, we can see that the overall performance of convergence time is almost the same for the two schemes. This can be attributed to

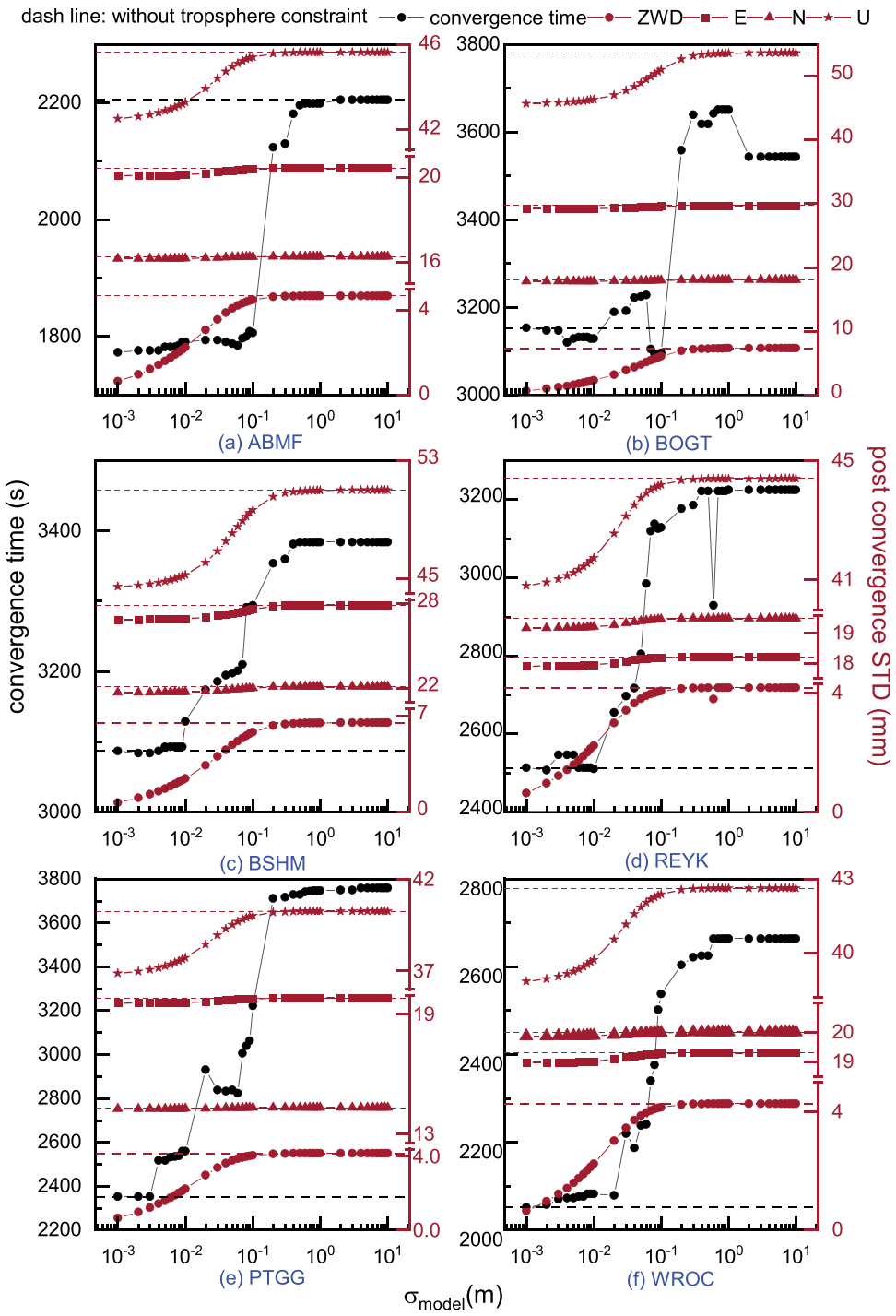

Figure 8. Convergence time (black line, left *y* axis, in seconds), post-convergence STD (including ZWD, E, N and U. Red line, right *y* axis, in millimeters) as a function of the priori STD of simulated tropospheric ground truth in the troposphere-weighted PPP.

the poorly considered accuracy of tropospheric constraints.

Based on the analysis above, the accuracy of the tropospheric constraint at each epoch varies across different stations due to the effects of interpolation and differences in ZTD forecast accuracy. To conduct a more comprehensive analysis of the overall improvement performance, GPS dual-frequency observation data from about 200 global IGS stations on day of year (DOY) 001 in 2022 were collected, and its distribution is shown in Figure 10. At each station, we first calculate out RMSE of the constrained ZWD series. Then, the two kinematic PPP schemes (standard PPP and troposphere-weighted PPP) were performed, and their convergence time difference was calculated. The predefined error threshold for convergence time was adjusted to 2 decimeters to accommodate the transition from static to kinematic mode. The distribution of the constrained ZWD accuracy and its improvement in convergence time is illustrated in the boxplot in Figure 11. As shown in Figure 11, the mean interpolated ZWD accuracy is 12 mm, which is

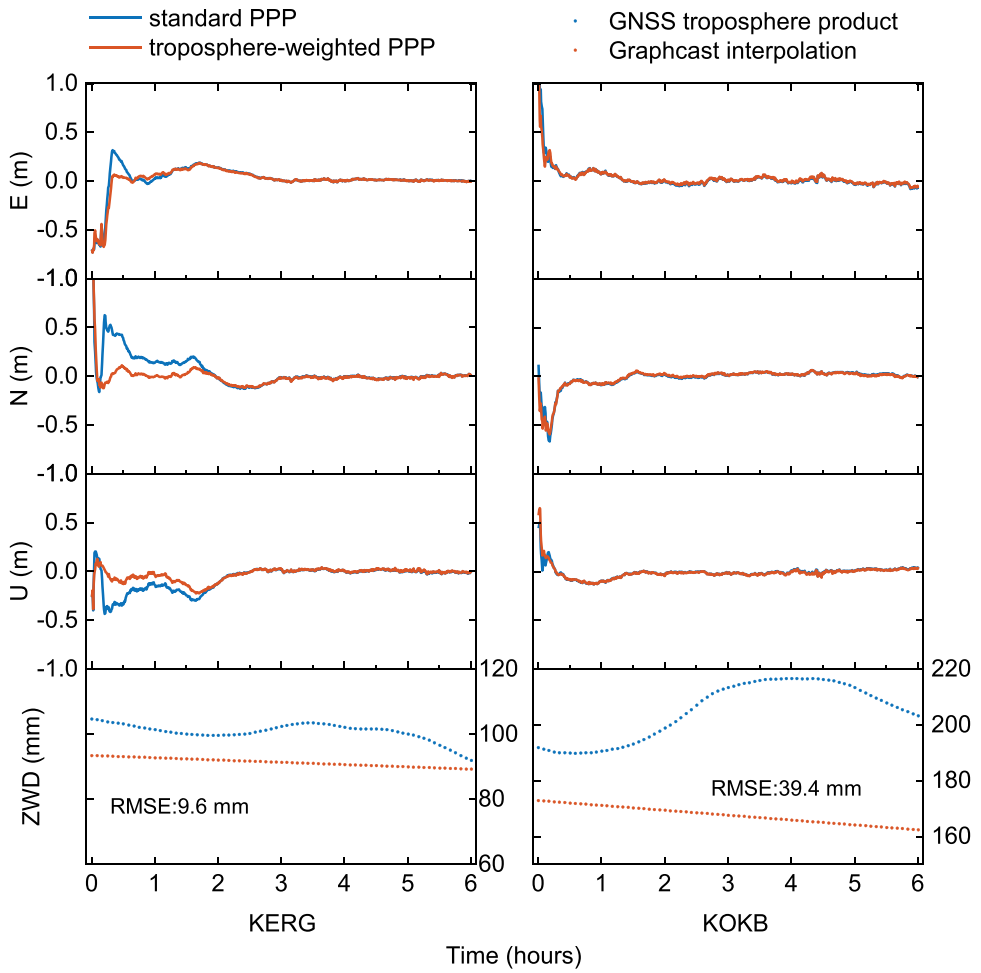

Figure 9. Performance comparison of standard PPP and troposphere-weighted PPP at station KERG (left) and KOKB (right) on January 1, 2022 (at the top three panels for east, north and up, respectively). The bottom panel shows priori troposphere information interpolated by GraphCast short-range forecast for the troposphere-weighted PPP, and its comparison with GNSS troposphere product.

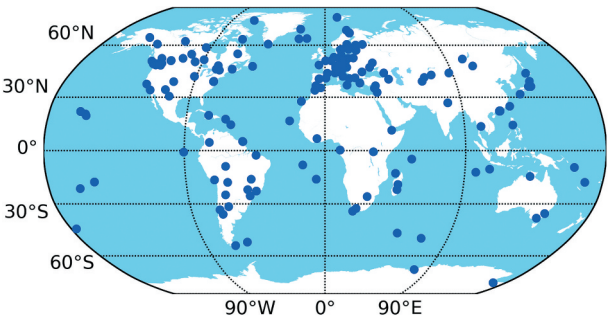

Figure 10. Distribution of the contributing IGS stations.

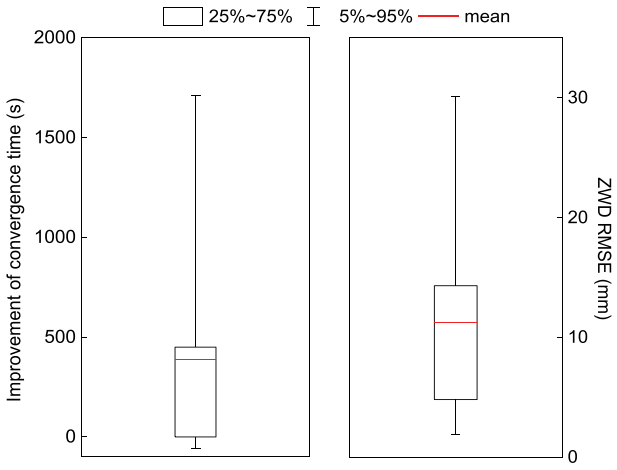

Figure 11. Boxplot of interpolated ZWD accuracy during positioning (right panel) and its improvement for convergence time (left panel) for about 200 stations.

compatible with the previous short-range troposphere delay forecast evaluation section. This also indicates that the troposphere variation remains stable at most stations within a 6-h time frame. On average, the improvement in convergence time is approximately 400 s. This finding agrees with results from the previous simulation experiment, which demonstrated similar reductions in convergence time. However, it is worth noting that the results of 25th percentile, which is around zero, suggests that certain stations did not show a significant improvement in the convergence time with the implementation of the troposphere constraints. In addition to the accuracy of constrained ZWD, this could be attributed to other factors such as satellite geometry and weather conditions specific to those stations. These factors have

a strong influence on the accuracy of ZWD estimation during the convergence period of PPP. When the accuracy of the estimated ZWD surpasses that of the external ZWD constraints, the influence of these external constraints gradually diminishes.

6.2. PPP augmented by medium-range forecast

Although short-range NWP offers more accurate tropospheric delays than medium-range forecasting, short-term forecasts may be impractical in engineering applications due to the unavailability or incompleteness of recent data. In such situations, medium-range forecasts, which utilize older data, can serve as an alternative approach to provide the required prior tropospheric delay. Despite the ZTD forecast accuracy being degraded to 4 cm with increasing prediction time, as mentioned earlier, there is still a possibility that the accuracy of tropospheric constraints higher than 1 decimeter can offer benefits for PPP convergence, provided that a proper stochastic model is applied.

The Chinese Hong Kong region experiences frequent extreme weather conditions, characterized by relatively high levels of water vapor throughout the year, which pose considerable challenges for accurate tropospheric delay prediction (Yang et al. 2023; Yu and Liu 2021). Therefore, we select the Hong Kong Continuous Operating Reference Station (CORS) network as a case study to evaluate the performance of troposphere-weighted PPP using medium-range forecast tropospheric delay. The used Hong Kong CORS network, comprising 17 stations, is shown in Figure 12, and the data collection period started on the 1st day of each month, continued for the following 10 days throughout the year 2022. The 10-day forecast horizon for positioning experiments was chosen because data-driven NWP models lose accuracy beyond this period, making them comparable to empirical models like GPT3, and because 10 days allow

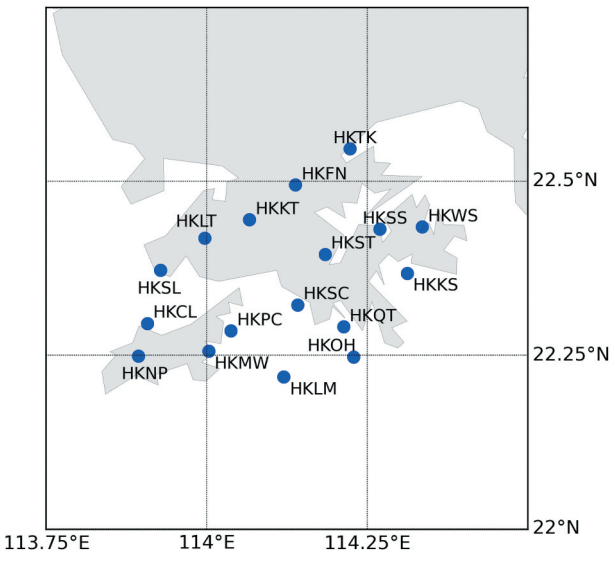

Figure 12. Distribution of the Hong Kong CORS network.

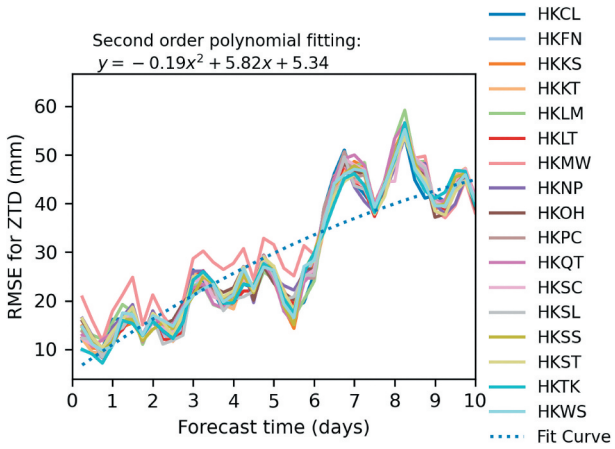

Figure 13. ZTD RMSE as a function of prediction time for 17 Hong Kong stations and its second order polynomial fitting function.

sufficient time for preparing initial weather forecast data. During this period, PPP filter was reinitialized every 2 h and the tropospheric delays at the 17 hK CORS stations were generated by the GraphCast model, which initialize at the 00z on the first day with a time step of 6 h. Figure 13 displays the RMSE of the generated ZTD as a function of prediction time for each station. It is evident that ZTD accuracy function of the entire Hong Kong CORS shows a consistent variation. By fitting a second-order polynomial function, we can determine the σ_{model} of ZTD as function of prediction time in the Hong Kong region. Applying the medium range forecast ZTD products with σ_{model} in the two compared PPP schemes, the improvement of convergence time is calculated and presented in Figure 14. Taking stations HKLM and HKMW as examples, the overall performance of convergence time improvement deteriorated with an increase in forecast time, with the presence of some outliers. As mentioned before, the application of troposphere constraints may sometimes not result in improvements. Therefore, to further assess the effect of constraints, we calculated the ratio of improvement part in all datasets and the mean improvement in convergence time for all 17 Hong Kong stations and show them in the bottom panel. The mean improvement in convergence time can reach up to 400 s within a 3-day forecast period, but it decreases to above 100 s as the forecast time increases. The improvement ratio exhibits similar varying characteristics, decreasing from 60% to 30% accordingly. This analysis suggests that even if prior tropospheric constraints have slightly lower accuracy, they can still provide benefits as long as a proper stochastic model is used.

7. Conclusions and outlook

This study underscores the significant potential of data-driven NWP models, such as Pangu-Weather, FengWu, and GraphCast, in enhancing PPP by providing accurate prior tropospheric information.

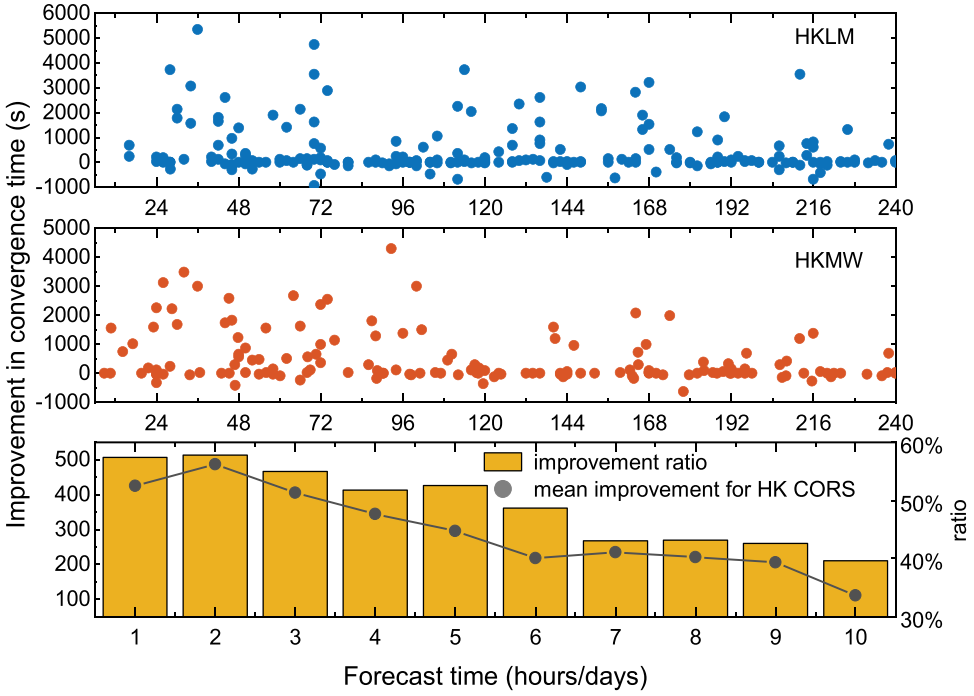

Figure 14. Improvement of convergence time applying tropospheric delay with different forecast times. Top and middle: performance for HKLM and HKMW. Bottom: statistics for the 17 Hong Kong CORS stations.

Comprehensive simulation experiments confirm that tropospheric uncertainty substantially affects PPP convergence time, with constraints exceeding 1 decimeter in accuracy yielding considerable benefits. Our evaluation of RWPN estimation indicates the feasibility of integrating this process into the existing data-driven NWP framework.

Further analysis of short- and medium-range ZTD forecasts shows that data-driven NWP models can generate accurate local forecasts within seconds. Their short-range ZTD forecasts consistently outperform those from the traditional GFS model. Residual analysis reveals that the accuracy of data-driven forecasts is sensitive to initial weather conditions; intense convection increases free tropospheric moisture, leading to greater instability and forecast errors. Seasonal and regional variations are evident: forecast accuracy tends to be higher in winter than in summer, with polar regions performing best, followed by tropical and mid-latitude regions.

Data from approximately 200 global IGS stations confirm that improvements in PPP performance are closely linked to the accuracy of tropospheric constraints, with an average convergence time reduction of about 400 s. In medium-range ZTD forecasting, data-driven models consistently surpass GFS, with FengWu yielding the best performance and Pangu-Weather the lowest. GraphCast and FengWu maintain ZTD forecast accuracy within 2 cm for up to 4 days, enabling extended preparation of initial conditions. Results from 17 hong Kong CORS stations further show that PPP can be significantly enhanced using short- to medium-range forecasts from data-driven global weather models, achieving mean convergence time improvements of up to 400 s within a three-day forecast window. These findings underscore the transformative potential of data-driven NWP models in advancing PPP and improving tropospheric forecasts. While these findings underscore the transformative potential of data-driven NWP for PPP and tropospheric forecasting, the current reliance on ERA5 initial conditions – which incur a roughly five-day latency – and six-hour, ~0.25° forecast resolution limit real-time applicability and the ability to capture fine-scale atmospheric variability. Moreover, the performance of data-driven NWP forecasts under different weather conditions (e.g. normal, rainy, and extreme weather) remains insufficiently characterized. Future research should therefore analyze forecast accuracy across these meteorological regimes and integrate higher-frequency numerical weather model outputs into data-driven NWP frameworks, fusing them with near-real-time GNSS-derived ZTD constraints. Such a hybrid approach will enhance the temporal and spatial fidelity of tropospheric constraints, thereby enabling practical, operational real-time PPP.

Data and code availability

GFS datasets were obtained from https://rda.ucar.edu/datasets/ds084.1/dataaccess/. The dataset of pressure levels and single levels of ERA5 datasets can be found on https://cds.climate.copernicus.eu/cdsapp#!/dataset/reanalysis-era5-pressure-levels?tab. =overview and https://cds.climate.copernicus.eu/cdsapp#!/dataset/rea

nalysis-era5-single-levels?tab=form. The inference code and pre-trained model of Pangu-weather, GraphCast and FengWu are available respectively at https://github.com/198808xc/Pangu-Weather., https://github.com/google-deepmind/graphcast., and https://github. com/OpenEarthLab/FengWu. NGL tropospheric delay products are available at http://geodesy.unr.edu/gps_timeseries/trop. The source code of GPT3 and GRM can be found at https://vmf.geo.tuwien.ac.at/codes. and https://zenodo.org/records/6967015, respectively. The source code of RADIATE can be found at https://github.co m/TUW-VieVS/RADIATE.git. The rapid products provided by Wuhan University are available at http://igs.gnsswhu.cn/pub/whu/phasebias.

Disclosure statement

No potential conflict of interest was reported by the author(s).

Funding

This work was supported in part by the University Grants Committee of Hong Kong under the General Research Fund (GRF) [Grant No. 15229622], the National Natural Science Foundation of China [Grant Nos. 42404052 and 42274017], Guangdong Basic and Applied Basic Research Foundation (Grant No. 2023A1515030184).

Notes on contributors

Yuanfan Deng received the B.S. and M.S. degrees from the School of Geodesy and Geomatics, Wuhan University, Wuhan, China, in 2019 and 2022, respectively. He is currently pursuing a Ph.D. degree in the Department of Land Surveying and Geoinformatics at The Hong Kong Polytechnic University, Hong Kong, China. His research focuses on precise GNSS positioning.

Wu Chen received the Ph.D. degree from Newcastle University, Newcastle upon Tyne, U.K., in 1992. He is currently a Professor with the Department of Land Surveying and Geo-Informatics, The Hong Kong Polytechnic University, Hong Kong, China. He has been actively working on GNSS-related research for more than 30 years. His main research interests include GNSS positioning quality evaluation, system integrity, various GNSS applications, seamless positioning, and simultaneous localization and mapping.

Junsheng Ding received the bachelor's degree from Chang'an University, Xi'an, China, in 2018, and the joint Ph.D. degree from Shanghai Astronomical Observatory, Chinese Academy of Sciences, Beijing, China, and the School of Astronomy and Space Science, University of Chinese Academy of Sciences, Beijing, in 2023. He is currently a Post-Doctoral Fellow with the Department of Land Surveying and Geo-Informatics, The Hong Kong Polytechnic University, Hong Kong, China. His research interests include GNSS meteorology and artificial intelligence for geodesy.

Ahmed El-Mowafy is Professor of Positioning and Navigation and Director of Graduate Research, School of Earth and Planetary Sciences, Curtin University, Australia. He obtained his Ph.D. from the University of Calgary, Canada. He has extensive publications in precise positioning and navigation using GNSS, quality control, integrity monitoring and estimation theory.

Duojie Weng received the B.S. and M.S. degrees in electrical engineering from Hohai University, Nanjing, China in 2007 and 2010, and the Ph.D. degree from The Hong Kong Polytechnic University, Hong Kong, China in 2016. He is currently a Research Assistant Professor with the Department of Land Surveying and Geo-Informatics, The Hong Kong Polytechnic University, Hong Kong China. His research interests include urban positioning, integrity monitoring of GNSS, Kinematic GPS, sensor integration for various navigation systems.

Long Tang received a Ph.D. degree in geodesy and surveying engineering from Wuhan University in 2015 and is an associate professor at the Guangdong University of Technology. His current research interests include GNSS precise positioning and ionospheric monitoring.

Lei Bai was a Post-Doctoral Research Fellow at The University of Sydney, Sydney, NSW, Australia. He is currently a Research Scientist with Shanghai AI Laboratory, Shanghai, China. He is leading the OpenEarthLab. His research interests include machine learning, spatial–temporal learning, and their applications. Dr. Bai was a recipient of the 2020 Google Ph.D. Fellowship, the 2020 UNSW Engineering Excellence Award, and the 2021 Dean's Award for Outstanding Ph.D. Theses.

Xiaolong Mi received the Ph.D. degree from the University of Chinese Academy of Sciences, Beijing, China, in 2022, and the Ph.D. degree from Curtin University, Perth, WA, Australia, in 2023. He is a Research Assistant Professor with the Department of Land Surveying and Geo-Informatics, The Hong Kong Polytechnic University, Hong Kong, China. His research interests include GNSS and low Earth orbit (LEO) technologies for positioning, navigation and timing (PNT), along with the application of AI in Earth and space sciences.

ORCID

Xiaolong Mi http://orcid.org/0000-0003-2950-3472

References

Hofmeister, A. 2016. Determination of path delays in the atmosphere for geodetic VLBI by means of ray-tracing

Bauer, P., A. Thorpe, and G. Brunet. 2015. "The Quiet Revolution of Numerical Weather Prediction." *Nature* 525 (7567): 47–55. https://doi.org/10.1038/nature14956.

Ben Bouallègue, Z., M. C. A. Clare, L. Magnusson, E. Gascón, M. Maier-Gerber, M. Janoušek, M. Rodwell, F. Pinault, J. S. Dramsch, S. T. K. Lang. 2024. "The Rise of data-Driven Weather Forecasting: A First Statistical Assessment of Machine learning–Based Weather Forecasts in an operational-Like Context." *Bulletin of the American Meteorological Society* [Internet]. [105 (6): E864–E883. Accessed May 22, 2024. https://doi.org/10.1175/BAMS-D-23-0162.1.

Bi, K., L. Xie, H. Zhang, X. Chen, X. Gu, and Q. Tian. 2023. "Accurate Medium-Range Global Weather Forecasting with 3D Neural Networks." *Nature* 619 (7970): 533–538. https://doi.org/10.1038/s41586-023-06185-3.

Black, H. D. 1978. "An Easily Implemented Algorithm for the Tropospheric Range Correction." *Journal of Geophysical Research Solid Earth* 83 (B4): 1825–1828. https://doi.org/10.1029/JB083iB04p01825.

Blewitt, G., W. Hammond, and C. Kreemer. 2018. "Harnessing the GPS Data Explosion for Interdisciplinary Science." *Eos* 99 (2): e2020943118. https://doi.org/10.1029/2018EO104623.

Chen, J., and Y. Gao. 2024. "A Machine learning-Based Tropospheric Prediction Approach for high-Precision real-Time GNSS Positioning." *Sensors (Switzerland)* 24 (10): 2957. https://doi.org/10.3390/s24102957.

Chen, K., T. Han, J. Gong, L. Bai, F. Ling, J.-J. Luo, X. Chen, L. Ma, T. Zhang, R. Su, et al. 2023. "Fengwu: Pushing the Skillful Global Medium-Range Weather Forecast Beyond 10 Days Lead." *ArXiv E-Prints.:arXiv:2304.02948*. https://doi.org/10.48550/arXiv.2304.02948.

Dodson, A., P. Shardlow, L. Hubbard, G. Elgered, and P. Jarlemark. 1996. "Wet Tropospheric Effects on Precise Relative GPS Height Determination." *Journal of Geodesy* 70 (4): 188–202. https://doi.org/10.1007/BF00873700.

Du, Z., Q. Zhao, Y. Yao, and H. Zhu. 2024. "Real-Time Tropospheric Delay Map Retrieval Using Sparse GNSS Stations." *GPS Solutions* 28 (1): 12. https://doi.org/10.1007/s10291-023-01554-x.

Elsobeiey, M. E. 2020. "Characteristic Differences Between IGS Final and ray-Traced Tropospheric Delays and Their Impact on Precise Point Positioning and Tropospheric Delay Estimates." *GPS Solutions* 24 (4): 97. https://doi.org/10.1007/s10291-020-01012-y.

Gao, R., Z. Liu, R. Odolinski, and B. Zhang. 2024. "Improving GNSS ppp-Rtk Through Global Forecast System Zenith Wet Delay Augmentation." *GPS Solutions* 28 (2): 66. https://doi.org/10.1007/s10291-023-01608-0.

Gong, Y., Z. Liu, S. Yu, P. W. Chan, and K. K. Hon. 2024. "Improving GNSS PPP Performance in the South China Under Different Weather Conditions by Using the Weather Research and Forecasting (WRF) model-Derived Wet Delay Corrections." *Earth & Space Science* 11 (3): e2023EA003136. https://doi.org/10.1029/2023EA003136.

Hackman, C., G. Guerova, S. Byram, J. Dousa, and U. Hugentobler. 2015. "International GNSS Service (IGS) Troposphere Products and Working Group Activities." Sofia, Bulgaria, 17–21 May 2015, edited by International Federation of Surveyors (FIG), 1–14. Openhagen, Denmark.

Hadas, T., F. N. Teferle, K. Kazmierski, P. Hordyniec, and J. Bosy. 2017. "Optimum Stochastic Modeling for GNSS Tropospheric Delay Estimation in Real-Time." *GPS Solutions* 21 (3): 1069–1081. https://doi.org/10.1007/s10291-016-0595-0.

Haji-Aghajany, S., Y. Amerian, S. Verhagen, W. Rohm, and H. Schuh. 2021. "The Effect of function-Based and Voxel-Based Tropospheric Tomography Techniques on the GNSS Positioning Accuracy." *Journal of Geodesy* 95 (7): 78. https://doi.org/10.1007/s00190-021-01528-2.

Haji-Aghajany, S., W. Rohm, T. Hadas, and J. Bosy. 2025. "Machine learning-Based Tropospheric Delay Prediction for real-Time Precise Point Positioning Under Extreme Weather Conditions." *GPS Solutions* 29 (1): 36. https://doi.org/10.1007/s10291-024-01782-9.

Haji-Aghajany, S., W. Rohm, P. Lipinski, and M. Kryza. 2024. "Beyond the Horizon: A Critical Analysis of ai-Based Weather Forecasting Models [Internet]. Accessed March 7, 2025. https://doi.org/10.22541/essoar.171632600.06154714/v1.

Hartmann, D. L., and M. L. Michelsen. 1993. "Large-Scale Effects on the Regulation of Tropical Sea Surface Temperature." *Journal of Climate* 6 (11): 2049–2062. https://doi.org/10.1175/1520-0442(1993)006<2049:LSEOTR>2.0.CO;2.

Hersbach, H., B. Bell, P. Berrisford, S. Hirahara, A. Horányi, J. Muñoz-Sabater, J. Nicolas, C. Peubey, R. Radu, and D. Schepers. 2020. "The ERA5 Global Reanalysis." *Quarterly Journal of the Royal Meteorological Society* 146 (730): 1999–2049. https://doi.org/10.1002/qj.3803.

Hobiger, T., R. Ichikawa, Y. Koyama, and T. Kondo. 2008. "Fast and Accurate Ray-Tracing Algorithms for Real-Time Space Geodetic Applications Using Numerical Weather Models." *Journal of Geophysical Research Atmospheres* [Internet]. 113(D20). 113 (D20). https://doi.org/10.1029/2008JD010503.

Hopfield, H. S. 1969. "Two-Quartic Tropospheric Refractivity Profile for Correcting Satellite Data." *Journal of Geophysical Research* 74 (18): 4487–4499. https://doi.org/10.1029/JC074i018p04487.

Huang, L., H. Bi, H. Zhang, S. Wang, F. Liao, L. Liu, and W. Jiang. 2024. "An Optimized BP Neural Network for Modeling Zenith Tropospheric Delay in the Chinese Mainland Using Coupled Particle Swarm and Genetic Algorithm." *Geo-Spatial Information Science*: 1–16. https://doi.org/10.1080/10095020.2024.2392701.

Huang, L., F. Liu, L. Guo, G. Lan, L. Zhou, C. Wang, and L. Liu. 2023. "An ERA5 Tropospheric parameters-Augmented Approach for Improving GNSS Precise Point Positioning." *Geodesy and Geodynamics* 14 (5): 467–476. https://doi.org/10.1016/j.geog.2023.01.004.

Hurter, F., and O. Maier. 2013. "Tropospheric Profiles of Wet Refractivity and Humidity from the Combination of Remote Sensing Data Sets and Measurements on the Ground." *Atmospheric Measurement Techniques* 6 (11): 3083–3098. https://doi.org/10.5194/amt-6-3083-2013.

Khutorov, V. E., G. M. Teptin, A. A. Zhuravlev, and O. G. Khutorova. 2016. "Variability of the tropospheric-Delay Temporal Structure Function of Radio Signals from the Global Navigation Satellite Systems versus Tropospheric Surface Layer Parameters." *Radiophysics Quantum Electronics* 59 (5): 352–360. https://doi.org/10.1007/s11141-016-9704-8.

Kouba, J., and P. Héroux. 2001. "Precise Point Positioning Using IGS Orbit and Clock Products." *GPS Solutions* 5 (2): 12–28. https://doi.org/10.1007/PL00012883.

Lam, R., A. Sanchez-Gonzalez, M. Willson, P. Wirnsberger, M. Fortunato, F. Alet, S. Ravuri, T. Ewalds, Z. Eaton-Rosen, W. Hu. 2023. "Learning Skillful medium-Range Global Weather Forecasting." *Science* 382 (6677): 1416–1421. https://doi.org/10.1126/science.adi2336.

Landskron, D., and J. Böhm. 2018. "VMF3/GPT3: Refined Discrete and Empirical Troposphere Mapping Functions." *Journal of Geodesy* 92 (4): 349–360. https://doi.org/10.1007/s00190-017-1066-2.

Li, H., G. Zhu, Q. Kang, L. Huang, and H. Wang. 2023. "A Global Zenith Tropospheric Delay Model with ERA5 and gnss-Based ZTD Difference Correction." *GPS*

Solutions 27 (3): 154. https://doi.org/10.1007/s10291-023-01503-8.

Li, X., X. Zhang, and M. Ge. 2011. "Regional Reference Network Augmented Precise Point Positioning for Instantaneous Ambiguity Resolution." *Journal of Geodesy* 85 (3): 151–158. https://doi.org/10.1007/s00190-010-0424-0.

Lu, C., X. Li, F. Zus, R. Heinkelmann, G. Dick, M. Ge, J. Wickert, and H. Schuh. 2017. "Improving beidou real-Time Precise Point Positioning with Numerical Weather Models." *Journal of Geodesy* 91 (9): 1019–1029. https://doi.org/10.1007/s00190-017-1005-2.

Nafisi, V., L. Urquhart, M. C. Santos, F. G. Nievinski, J. Bohm, D. D. Wijaya, H. Schuh, A. A. Ardalan, T. Hobiger, R. Ichikawa. 2012. "Comparison of ray-Tracing Packages for Troposphere Delays." *IEEE Transactions on Geoscience and Remote Sensing: A Publication of the IEEE Geoscience and Remote Sensing Society* 50 (2): 469–481. https://doi.org/10.1109/TGRS.2011.2160952.

National Centers for Environmental Prediction/National Weather Service/NOAA/U.S. Department of Commerce. 2015. NCEP GFS 0.25 Degree Global Forecast Grids Historical Archive. Research Data Archive at the National Center for Atmospheric Research, Computational and Information Systems Laboratory. *Dataset*. https://doi.org/10.5065/D65D8PWK

Nilsson, T., J. Böhm, D. D. Wijaya, A. Tresch, V. Nafisi, and H. Schuh. 2013. "Path Delays in the Neutral Atmosphere." In *Atmospheric Eff Space Geod [Internet]*, edited by J. Böhm and H. Schuh, 73–136. Berlin, Heidelberg: Springer Berlin Heidelberg. https://doi.org/10.1007/978-3-642-36932-2_3.

Rüeger, J. 2002. "Refractive Index Formulae for Electronic Distance Measurement with Radio and Millimetre Waves." *Unisurv Rep. S-68*, 1–52. Sydney: School of Surveying and Spatial Information Systems, Universtiy of New South Wales.

Saastamoinen, J. 1972. "Contributions to the Theory of Atmospheric Refraction." *Bulletin Géodésique* 105 (1): 279–298. https://doi.org/10.1007/BF02521844.

Vaclavovic, P., J. Dousa, M. Elias, and J. Kostelecky. 2017. "Using External Tropospheric Corrections to Improve GNSS Positioning of hot-Air Balloon." *GPS Solutions* 21 (4): 1479–1489. https://doi.org/10.1007/s10291-017-0628-3.

Wang, J., and Z. Liu. 2019. "Improving GNSS PPP Accuracy Through WVR PWV Augmentation." *Journal of Geodesy* 93 (9): 1685–1705. https://doi.org/10.1007/s00190-019-01278-2.

Wilgan, K., T. Hadas, P. Hordyniec, and J. Bosy. 2017. "real-Time Precise Point Positioning Augmented with high-Resolution Numerical Weather Prediction Model." *GPS Solutions* 21 (3): 1341–1353. https://doi.org/10.1007/s10291-017-0617-6.

Wu, Z., C. Lu, Y. Tan, Y. Zheng, Y. Liu, Y. Liu, and K. Jin. 2023. "Real-Time GNSS Tropospheric Delay Estimation with a Novel Global Random Walk Processing Noise Model (GRM)." *Journal of Geodesy* 97 (12): 112. https://doi.org/10.1007/s00190-023-01780-8.

Xia, P., M. Tong, S. Ye, J. Qian, and F. Hu. 2023. "Establishing a High-Precision Real-Time ZTD Model of China with GPS and ERA5 historical Data and Its Application in PPP." *GPS Solutions* 27 (1): 2. https://doi.org/10.1007/s10291-022-01338-9.

Xu, Y., X. Meng, J. Cui, and L. Ma. 2025. "A Regional Augmented PPP Algorithm for Offshore Considering NWP." *Geo-Spatial Information Science*: 1–14. https://doi.org/10.1080/10095020.2024.2441515.

Yang, F., X. Gong, Y. Wang, M. Liu, J. Li, T. Xu, and R. Hao. 2023. "GNSS Water Vapor Tomography Based on Kalman Filter with Optimized Noise Covariance." *GPS Solutions* 27 (4): 181. https://doi.org/10.1007/s10291-023-01517-2.

Yao, Y., W. Peng, C. Xu, and S. Cheng. 2017. "Enhancing real-Time Precise Point Positioning with Zenith Troposphere Delay Products and the Determination of Corresponding Tropospheric Stochastic Models." *Geophysical Journal International* 208 (2): 1217–1230. https://doi.org/10.1093/gji/ggw451.

Yu, S., and Z. Liu. 2021. "Tropical cyclone-Induced Periodical Positioning Disturbances During the 2017 hato in the Hong Kong Region." *GPS Solutions* 25 (3): 109. https://doi.org/10.1007/s10291-021-01112-3.

Zhang, H., Y. Yao, M. Hu, C. Xu, X. Su, D. Che, and W. Peng. 2022. "A Tropospheric Zenith Delay Forecasting Model Based on a Long short-Term Memory Neural Network and Its Impact on Precise Point Positioning." *Remote Sensing* 14 (23): 5921. https://doi.org/10.3390/rs14235921.

Zhang, H., Y. Yuan, and W. Li. 2022. "Real-Time wide-Area Precise Tropospheric Corrections (WAPTCs) Jointly Using GNSS and NWP Forecasts for China." *Journal of Geodesy* 96 (6): 44. https://doi.org/10.1007/s00190-022-01630-z.

Zhang, Z., Y. Lou, W. Zhang, Z. Wang, Y. Zhou, J. Bai, Z. Zhang, and C. Shi. 2023. "Dynamic Stochastic Model for Estimating GNSS Tropospheric Delays from Air-Borne Platforms." *GPS Solutions* 27 (1): 39. https://doi.org/10.1007/s10291-022-01375-4.

Zhou, Y., Y. Lou, W. Zhang, C. Kuang, W. Liu, and J. Bai. 2020. "Improved Performance of ERA5 in Global Tropospheric Delay Retrieval." *Journal of Geodesy* 94 (10): 103. https://doi.org/10.1007/s00190-020-01422-3.